Title：Dual targeting of astrocytic and endothelial GLUT1 enables functional rescue in GLUT1 deficiency syndrome

Shoko Tamura[1], Hiroko Shimbo[1], Nobuyuki Aruga[1,2], Haruo Okado[1], Erika Seki[3], Kazunari Sekiyama[3], Kenichi Oshima[4], Shinobu Hirai[1]*

1. Brain Metabolic Regulation Group, Department of Basic Medical Sciences, Tokyo Metropolitan Institute of Medical Science, Tokyo, Japan
2. Graduate School of Medical and Dental Sciences, Science Tokyo, Tokyo, Japan
3. Laboratory of Molecular Pathology and Histology, Center for Medical Research Cooperation, Tokyo Metropolitan Institute of Medical Science, Tokyo, Japan
4. Department of Psychiatry, Tokyo Metropolitan Matsuzawa Hospital, Tokyo, Japan

*Corresponding author: Shinobu Hirai

Brain Metabolic Regulation Group, Department of Psychiatry and Behavioral Sciences, Tokyo Metropolitan Institute of Medical Science, Tokyo, Japan
E-mail: hirai-sn@igakuken.or.jp
Tel: +81-03-5316-3100

Competing interests: The authors declare no competing interests.

Abstract

Glucose transporter 1 deficiency syndrome (GLUT1-DS) is a metabolic encephalopathy caused by impaired glucose transport into the brain. Although GLUT1 in brain microvascular endothelial cells at the blood-brain barrier has been recognized as essential for glucose transport into the brain, the role of astrocytic GLUT1 has remained uncertain, limiting progress in gene therapy for GLUT1-DS. Here we show that astrocytic GLUT1 is broadly expressed in both mouse and human brains and is indispensable for maintaining cerebrospinal fluid glucose, cognitive performance, and motor coordination. Conditional haploinsufficiency in either astrocytes or endothelial cells reproduced GLUT1-DS-like phenotypes, and full rescue required AAV-mediated GLUT1 restoration in both cell types. To this end, we developed AAV-AST, a blood-brain barrier-penetrant vector with strong astrocyte tropism, and identified a regulatory element (Region d) that recapitulates endogenous GLUT1 expression. Together, these findings establish dual targeting of astrocytic and endothelial GLUT1 as a rational therapeutic strategy, paving the way for next-generation therapies for GLUT1-DS and related neuro-metabolic disorders.

Introduction

The human brain, though comprising only ~2% of body mass, accounts for nearly 20% of systemic glucose utilization[1,2]. Glucose uptake in the brain is primarily mediated by facilitative glucose transporters (GLUTs), of which 14 isoforms exist in humans[3]. Among these, glucose transporter 1 (GLUT1) is the dominant isoform at the blood–brain barrier, expressed abundantly in vascular endothelial cells[4,5].

Reduced expression or function of GLUT1 causes GLUT1 deficiency syndrome (GLUT1-DS), a rare metabolic encephalopathy first described in 1991[6]. Heterozygous *SLC2A1* mutations underlie most cases[7], with an incidence estimated at 1 in 24,300–60,600 births[8,9]. Patients present with a broad spectrum of symptoms, including seizures, abnormal eye–head movements, cognitive and motor delay, and impaired head growth[10]. This clinical heterogeneity complicates diagnosis for GLUT1-DS, and the true prevalence is likely underestimated. A reduced cerebrospinal fluid (CSF)-to-blood glucose ratio is the key diagnostic hallmark, seen in nearly all patients[11,12].

Current therapy relies on ketogenic diets, which partially improve seizures and cognitive and motor dysfunction.[10,13,14]. Safety concerns remain, particularly during pregnancy[15]. These limitations underscore the urgent need for curative approaches. Gene therapy using adeno-associated virus (AAV) vectors has emerged as a promising strategy, with proof-of-concept studies demonstrating benefit in animal models[16-19]. Endothelial cells (ECs) have been considered the primary therapeutic target. This is based on the fact that GLUT1 expression has been classically regarded as selective to the capillary endothelium[5,20], and

that Glut1 deletion restricted to endothelial cells phenocopies systemic haploinsufficiency[17,21].

Nevertheless, evidence suggests that GLUT1 expression is not confined to ECs. Spatial transcriptomic datasets report Glut1 mRNA expression in microglia, oligodendrocytes, astrocytes, and neurons, although the corresponding protein distribution remains unclear (https://www.proteinatlas.org/). Several studies described astrocytic GLUT1 protein [22-24], but these findings were inconsistent and difficult to interpret given the limited resolution of early staining approaches. Astrocytes are thought to support neural activity through metabolic coupling, in which intracellularly imported glucose is converted to lactate and supplied to neurons via the astrocyte–neuron lactate shuttle [2,25,26]. The prevailing model has been that astrocytic GLUT1 is concentrated in perivascular endfeet for lactate production.

Here we show, using a mouse model, that astrocytic GLUT1 is required for glucose entry into the brain parenchyma and for maintaining brain glucose homeostasis, suggesting that effective therapy for GLUT1-DS may require restoring GLUT1 in both endothelial and astrocytic compartments. However, astrocytes remain difficult to transduce, as conventional AAV serotypes preferentially target neurons or endothelium while transducing astrocytes inefficiently[27,28]. In parallel, precise transcriptional regulatory elements are needed to restrict therapeutic GLUT1 expression to relevant cell types. We therefore delineate the roles of endothelial and astrocytic GLUT1 and develop an astrocyte-tropic AAV platform and regulatory element to enable rational dual targeting and functional rescue.

Results

GLUT1 is expressed in both endothelial cells and astrocytes in mouse and human brains

We first assessed the cellular distribution of Glut1 (GLUT1) in the mouse and human brain. In mice, Glut1 was abundantly expressed across the brain parenchyma (Fig. 1A). While conventional immunohistochemistry primarily localized Glut1 to vascular ECs, enhanced detection with the avidin–biotin complex (ABC) method revealed extensive expression in astrocytes as well. Notably, the labeling extended continuously from perivascular endfeet along the soma to distal astrocytic processes (Fig. 1B). Similarly, in the human postmortem brains, GLUT1 was strongly expressed in ECs and more weakly but broadly in astrocytes (Fig. 1C). These findings indicate that astrocytic GLUT1 expression is not confined to perivascular regions but is distributed throughout the entire astrocytic soma and processes.

Both astrocytic and endothelial GLUT1 deficiency contribute to cognitive and motor impairments

To determine the functional relevance of astrocytic GLUT1, we compared systemic Glut1 heterozygous mice (Glut1 del/+) with conditional heterozygotes lacking one allele in astrocytes (Aldh1l1-Cre; Glut1 flox/+) or ECs (Tie2-Cre; Glut1 flox/+) (Fig. 2). Systemic Glut1 del/+ mice have been reported to show cognitive impairments resembling those in GLUT1 deficiency syndrome (GLUT1-DS) patients[21]. In both the object location test (OLT) and novel object recognition test (NORT), astrocyte-specific and EC-specific heterozygotes displayed significantly lower discrimination index scores than wild-type (WT) controls (OLT: $p < 0.0001$ and $p = 0.0002$; NORT: $p = 0.0012$ for both), closely paralleling deficits in Glut1 del/+ mice (Fig. 2A, B).

Motor coordination, a hallmark deficit in GLUT1-DS, was then evaluated using the slip test. As previously reported, EC-specific Glut1 deficiency impairs rotarod performance[17], Consistent with this**,** EC-specific heterozygotes showed significant deficits compared with WT controls, and notably, astrocyte-specific heterozygotes exhibited comparable impairments ($p < 0.0001$, $p = 0.0006$, and $p = 0.0180$, respectively) (Fig. 2C). Together, these results indicate that both astrocytic and endothelial GLUT1 are indispensable for maintaining normal cognitive and motor functions.

Glut1 deficiency in astrocytes and ECs lowers CSF-to-blood glucose ratio **without altering blood glucose**

Because a reduced cerebrospinal fluid (CSF)-to-blood glucose ratio is a diagnostic hallmark of GLUT1-DS, we next assessed glucose concentrations (Fig. 2D). While blood glucose levels were unchanged across groups (Supplementary Fig. 1), CSF-to-blood glucose ratio was significantly reduced in Glut1 del/+, Aldh1l1-Cre; Glut1 flox/+, and Tie2-Cre; Glut1 flox/+ mice compared to WT controls ($p < 0.0001$ for each). These results confirm that GLUT1 in both astrocytes and ECs is necessary for sustaining CSF glucose homeostasis.

Both astrocytic and endothelial GLUT1 are required for brain glucose uptake

To directly evaluate brain glucose uptake, we monitored thalamic interstitial fluid (ISF) glucose concentrations after oral glucose administration (0.03 g per mouse) (Fig. 2E,F). Thalamic glucose uptake, as identified by [^18F]-FDG positron emission tomography, is known to be reduced in GLUT1-DS patients[29]. ISF glucose elevation was markedly attenuated in systemic, astrocyte-specific, and EC-specific Glut1 heterozygotes compared with WT controls ($p < 0.0001$ for each). These findings establish that astrocytic and endothelial GLUT1 jointly enable glucose entry into the brain parenchyma in response to systemic glucose fluctuations.

Development of AAV-AST: a BBB-penetrant vector with robust astrocyte tropism

To develop an astrocyte-targeted gene therapy approach, we rationally engineered an AAV-based capsid containing an optimized heptapeptide insertion within the VR-VIII loop. We reanalyzed previously published AAV insertion library datasets focusing on motifs enriched

in GFAP-positive astrocytes.[30-33] Position-specific frequency analysis identified a consensus sequence T(L/A/T) xxPF[K/L], with strong conservation of Thr at position 1 and Pro–Phe at positions 5–6. A sequence logo generated from 15 representative motifs revealed that, although the maximum information content was modest, the positional enrichment pattern remained visually distinct, delineating the T(L/A/T) xxPF[K/L] core architecture characteristic of astrocyte-tropic variants (Supplementary Fig. 2A).

From this integrated analysis, four high-scoring motifs were identified—TLAVPFK, TTLKPFL, TALKPFL, and TLQLPFK—with relative logo scores of 1.00, 0.92, 0.88, and 0.83, respectively (Supplementary Fig. 2B). Based on an empirical threshold (relative logo score ≥ 0.8; see Methods), three novel motifs (ranked 2nd–4th) were selected for *in vivo* validation. These were designated AAV-AST0 (TTLKPFL), AAV-AST1 (TALKPFL), and AAV-AST3 (TLQLPFK). All three retain the conserved consensus T(L/A/T) xxPF[K/L], while introducing subtle sequence divergence predicted to modulate astrocyte selectivity. The top-scoring motif, TLAVPFK, was excluded because it is identical to the PHP.eB insertion sequence.

To functionally validate these candidates, we performed intravenous administration in mice. AAV-AST0 failed to traverse the murine BBB and showed only limited CNS transduction (Supplementary Fig. 2C). In contrast, AAV-AST3 crossed the BBB and robustly transduced astrocytes, but it also transduced neurons at a similar magnitude, prompting us to exclude it from further analyses. (Supplementary Fig. 2D). Among the variants tested, AAV-AST1 displayed the most favorable profile, combining efficient BBB penetration with pronounced astrocyte selectivity. This screening yielded a variant capable of crossing the BBB, which we designated AAV-AST. We selected AAV-AST1 (TALKPFL insertion) as the lead candidate and hereafter refer to it as AAV-AST.

Following intravenous delivery, AAV-AST mediated widespread and efficient gene transfer throughout the brain, with a strong preference for astrocytes and minimal transduction of neurons and other CNS cell types (Fig. 3A). Astrocyte tropism was particularly pronounced in juvenile mice (Fig. 3B, C). We next evaluated transduction in primary human astrocytes. Compared with the control capsids AAV9 and PHP.eB, AAV-AST achieved significantly higher transduction efficiency (Fig. 3D–F). In mice, PHP.eB has been shown to efficiently cross the blood–brain barrier and enable widespread astrocyte transduction[34]. AAV9 is an AAV serotype currently used for intravenous gene therapy in human neurological diseases[35]. Together, these results suggest that AAV-AST represents a clinically relevant platform for astrocyte-directed gene delivery.

Targeting both astrocytes and ECs is necessary for effective GLUT1 gene therapy

To determine the extent to which dual targeting is required for phenotypic rescue, we performed intravenous rescue experiments in Glut1 del/+ mice using AAV vectors that preferentially transduce vascular endothelial cells (AAV-BR1[36] and AAV-X1.1[37]) and an astrocyte-tropic vector (AAV-AST). Vectors encoding GLUT1-myc-T2A-mCherry under the

CAG promoter were administered by retro-orbital injection between postnatal days 15 and 19 (P15–P19) (Supplementary Fig. 3), either to restore GLUT1 in a single cell type (endothelium or astrocytes) or simultaneously in both. In behavioral analyses, object location memory (OLT) was significantly improved by either endothelial- or astrocyte-directed supplementation, whereas the dual-targeting regimen produced the most pronounced rescue relative to vehicle-treated heterozygotes (Fig. 4A). Similarly, the CSF-to-blood glucose ratio was partially restored by single-cell-type supplementation and further enhanced by dual targeting, approaching wild-type levels (Fig. 4E). In contrast, in the novel object recognition test (NORT), single-cell-type supplementation did not produce a detectable rescue, whereas dual supplementation restored performance, indicating that concurrent restoration in both compartments is required for this cognitive domain (Fig. 4B). Motor coordination deficits assessed by the foot-slip test were not significantly improved in any rescue group compared with Glut1 del/+ controls under this treatment paradigm (Fig. 4C). Random-fed blood glucose remained unchanged across all viral and control groups (Fig. 4D).

Identification of a regulatory region enabling endogenous GLUT1 expression

Having established that optimal phenotypic rescue requires restoring GLUT1 in both endothelial cells and astrocytes, we next asked whether therapeutic expression could be placed under endogenous-like transcriptional control. We therefore prioritized candidate cis-regulatory elements at the *SLC2A1* (GLUT1) locus by integrating H3K27ac ChIP–seq tracks in the UCSC Genome Browser (https://genome.ucsc.edu/index.html), ENCODE-annotated candidate regions, and a previously reported *SLC2A1* regulatory sequence (Fig. 5A). Nine candidate sequences (a–i) were cloned upstream of an mCherry reporter and co-transfected with a CAG-GFP plasmid as a transfection control (Fig. 5B–D and Supplementary Fig. 4). In both human brain microvascular endothelial cells (hBMECs) (Fig. 5B,C) and primary cultured human astrocytes (Fig. 5D and Supplementary Fig. 4), only Region d exhibited reporter activity significantly higher than Ref. when quantified after normalization to CAG-GFP. These results identify Region d as a robust cis-regulatory element for driving *SLC2A1*-like expression and support its use in combination with endothelial- and astrocyte-tropic AAV vectors to implement dual-targeted GLUT1 supplementation.

***In vivo* validation of the regulatory activity of Region d**

To evaluate whether the regulatory activity of Region d identified in vitro is preserved in vivo, a reporter construct containing this regulatory element was packaged into an AAV-V1 capsid and systemically administered to mice by retro-orbital injection (Fig. 6A). To interrogate the function of the regulatory element using a single capsid, we chose AAV-V1, an AAV serotype capable of transducing both vascular endothelial cells and astrocytes in mice[31]. Region d drove reporter expression confined to vascular endothelial cells and astrocytes, faithfully recapitulating the endogenous *SLC2A1* (GLUT1) expression pattern, although overall transduction efficiency remained low.

To enhance expression strength without altering cell-type specificity, a CMV enhancer was placed upstream of Region d[38] **(**hereafter referred to as Region d′**;** Fig. 6B). This modification markedly increased the number of mCherry-positive cells in both vascular endothelial cells and astrocytes, yielding a signal distribution and intensity that more closely resembled endogenous GLUT1 expression.
Together with the in vitro results, these data establish Region d as a potent cis-regulatory element capable of conferring endogenous-like *SLC2A1* expression, providing a molecular foundation for AAV-based gene therapy strategies targeting both vascular endothelial cells and astrocytes.

Discussion

In this study, we provide direct evidence that GLUT1 is expressed not only in vascular endothelial cells (ECs) but also widely in astrocytes in human and mouse brains. This distribution extends well beyond perivascular endfeet, underscoring that astrocytes, long considered metabolic supporters, are themselves central to brain glucose homeostasis (Supplementary Fig. 5). Functionally, we demonstrate that reduction of Glut1 expression in either ECs or astrocytes alone was sufficient to induce phenotypes closely resembling GLUT1 deficiency syndrome (GLUT1-DS), including cognitive and motor impairments as well as reductions in cerebrospinal fluid (CSF)-to-blood glucose ratios. These findings establish that both astrocytic and endothelial GLUT1 are indispensable for maintaining brain metabolism and function.

Previous spatial transcriptomic datasets have shown that Glut1 mRNA is expressed in multiple non-endothelial cell types, in addition to endothelial cells (https://www.proteinatlas.org/), and protein-level detection primarily in ECs by using immunoblotting and immunohistochemistry[5,20]. Astrocytic GLUT1 has been thought to localize mainly at perivascular endfeet[5,22]. By integrating these fragmented observations, our study demonstrates widespread GLUT1 distribution throughout astrocytic membranes in both human and mouse brains (Fig. 1). Interestingly, in mice, all genetically labeled astrocytes expressed GLUT1, whereas in human brains, some astrocytes expressed GLUT1 while others did not, consistent with the evolutionary expansion of astrocytic diversity[39,40]. These results suggest that human astrocytes may exhibit more specialized metabolic subtypes than those in rodents.

Systemic Glut1 heterozygous mice recapitulate cardinal features of GLUT1-DS, including reduced CSF-to-blood glucose ratios and impaired neurodevelopment, motor coordination, and seizure susceptibility[41]. EC-specific Glut1 heterozygotes similarly display reduced CSF glucose and motor impairments[4,17]. Extending these findings, we show here that astrocyte-specific heterozygotes also develop cognitive and motor deficits with decreased CSF-to-blood glucose ratios, thereby highlighting that astrocytic Glut1 contributes as critically as endothelial Glut1 to GLUT1-DS pathogenesis (Fig. 2).

Mechanistically, astrocytes take up glucose through their perivascular endfeet and metabolize it into lactate, regulating extracellular lactate concentrations through monocarboxylate transporter 1 (MCT1) and contributing to the astrocyte–neuron lactate shuttle[1,2,25,26]. On the other hand, glucose itself is present in the extracellular space and has been measured via microdialysis[42,43]. Neurons take up glucose not only through lactate but also primarily via GLUT3 and GLUT4, the latter translocating to neuronal membranes during some activities[44,45]. Our biosensor-based analysis demonstrated that oral glucose uptake into the brain parenchyma was significantly impaired in systemic, EC-specific, and astrocyte-specific Glut1 heterozygotes (Fig. 2). Together, these findings suggest that extracellular glucose is also regulated by astrocytes, consistent with the distribution of GLUT1 across astrocytic membranes. Because GLUT1 operates as a facilitated transporter, astrocytes may mediate bidirectional glucose transport, coupling intracellular and extracellular gradients[46]. Given the close exchange between CSF and interstitial fluid[47], reductions in CSF glucose likely reflect impaired parenchymal glucose supply.

From a therapeutic perspective, the ketogenic diet remains the standard of care for GLUT1-DS, but its efficacy for cognitive and motor impairments is limited[48]. Consequently, gene therapy approaches using AAV vectors have been pursued[16,18,49]. Our findings show that restoring GLUT1 in either astrocytes or ECs alone was insufficient for robust recovery, whereas dual targeting achieved substantial functional improvement, normalizing the CSF-to-blood glucose ratio and ameliorating cognitive deficits (Fig. 4). This underscores that successful gene therapy must simultaneously address both cell types.
Notably, motor coordination was not rescued under our treatment paradigm, consistent with previous work showing that later interventions fail to restore motor function[19]. This aligns with evidence that motor phenotypes arise from early-life glucose insufficiency and that treatment efficacy is strongly dependent on the developmental stage at initiation[17,48,50]. Thus, earlier intervention may be necessary to fully rescue motor outcomes in GLUT1-DS, paralleling the high glucose demand of the developing human brain[51].

One of the major challenges in CNS gene therapy is the reproduction of endogenous expression patterns in target cell types following systemic delivery. Our study identifies regulatory Region d as a critical enhancer that faithfully mirrors endogenous GLUT1 expression in both ECs and astrocytes (Fig. 5, 6 and Supplementary Fig. 4), addressing this key limitation. To achieve such dual targeting, complementary vector systems are required. X1.1, developed by others, has been experimentally demonstrated to efficiently transduce human vascular endothelial cells[37], whereas our newly developed AAV-AST mediates robust and preferential transduction of astrocytes (Fig. 3 and Supplementary Fig. 2). When combined with Region d or Region d' (CMV–Region d), coordinated use of X1.1 and AAV-AST provides a modular route toward endogenous-like GLUT1 expression across both cell types, forming a versatile platform for dual-targeted supplementation. Collectively, these findings support astrocyte-targeted gene therapy for GLUT1-DS and potentially a broader spectrum of astrocyte-related diseases. By enabling rationally engineered dual-targeting

strategies, our work charts a path toward clinical translation of AAV-based therapies that harness astrocytes as active therapeutic targets.

Conclusion

In summary, we demonstrate that both astrocytic and endothelial GLUT1 are indispensable for maintaining brain glucose homeostasis and preventing the neurobehavioral phenotypes characteristic of GLUT1-DS. Our findings reveal that effective therapy requires dual targeting of these two cell types, a goal that can now be pursued by combining a newly identified regulatory element (Region d) with the next-generation astrocyte-tropic vector AAV-AST. This dual-platform strategy addresses key barriers in CNS gene therapy and highlights a path in which astrocytes can be harnessed as direct therapeutic targets. Beyond GLUT1-DS, this paradigm holds broad promise for a wide spectrum of astrocyte-related neurological disorders, offering a clear path from proof-of-concept toward clinical development.

Methods

Human postmortem brain tissue collection

Human postmortem brain tissues were obtained from the Tokyo Metropolitan Matsuzawa Hospital. The use of postmortem human brain tissues in the present study was approved by the Ethics Committee of Tokyo Metropolitan Institute of Medical Science (no. 23-26) and complied with the Declaration of Helsinki and its later amendments. All procedures were conducted with the informed written consent of the next of kin.

Immunohistochemistry of Postmortem Brain Tissue

Tissue sections were permeabilized with PBS containing 0.3% Triton X-100 for 30 min at room temperature (R.T.), followed by quenching of endogenous peroxidase activity with 1% aqueous hydrogen peroxide for 20 min. Heat-induced antigen retrieval was performed in Tris-HCl buffer (pH 9.5) at 98°C for 1 hour. After blocking with 10% normal goat serum in PBS containing 0.3% Triton X-100 for 1 hour, sections were incubated overnight at 4°C with primary antibodies against GLUT1 (rabbit; 1:200, Frontier Institute Co.,Ltd., Af610) and GLT-1 (guinea pig; 1:200, Millipore, A1783).
Following three washes in PBS containing 0.3% Triton X-100, sections were incubated for 2 hours at RT with biotinylated goat anti-rabbit IgG (1:1000, Vector, BA-1000) to detect GLUT1. After another set of washes, signal amplification was performed using the VECTASTAIN Elite ABC Kit (PK-6100) for 30 min. Sections were then blocked with 5% normal donkey serum in PBS containing 0.3% Triton X-100 for 15 min, followed by TrueBlack® Lipofuscin Autofluorescence Quencher (5% in 70% ethanol, Cosmo Bio, Tokyo, Japan) treatment for 30 sec.

For fluorescence detection, GLUT1 signal was developed with TSA-Cy5 (1:500) for 10 min. Sections were then incubated with donkey anti–guinea pig IgG Cy3 (1:500, Merck Millipore, AP193C) to detect GLT-1, together with DAPI (1:100, Dojindo, D523) for 2 hours at RT. After final washes, sections were mounted with fluorescence mounting medium.

Animals

All experimental procedures were approved by the Animal Experimentation Ethics Committee of the Tokyo Metropolitan Institute of Medical Science (No. 24-034, approved on 1 April 2024). Animal care was provided in accordance with the institutional animal experimentation guidelines. All mice were maintained under controlled temperature (23 ± 1 °C), humidity (50 ± 10%), and 12:12 h light/dark cycle (lights on at 8:00 a.m.) with free access to a standard laboratory diet and water. All efforts were made to minimize the number of animals used and their suffering. Glut1 heterozygous mutant (Glut1 del/+) mice, used as a model for Glut1 deficiency syndrome (Glut1-DS)[41], were generated by crossing CAG-Cre mice (a kind gift from Dr. Murakami[52]) with floxed Glut1 mice (The Jackson Laboratory, stock no. 031871). This cross results in Cre-mediated deletion of the floxed Glut1 gene in oocytes, leading to systemic Glut1 deficiency in the offspring. Mice harboring the Tie2-Cre (stock no. #004128), Aldh1l1-Cre (stock no. #023748), Aldh1l1-CreERT2 (stock no. #029655) drivers, tdTomato-floxed STOP reporter mice (tdTomato reporter mice) (stock no. 007914) and floxed Glut1 mice (stock no. #031871) were all obtained from the Jackson Laboratory, backcrossed over 10 generations to the C57BL/6J genetic strain background. Homozygous Glut1 flox/flox mice were mated with Tie2-Cre and Aldh1l1-Cre mice to generate Tie2-Cre; Glut1 flox/+ and Aldh1l1-Cre; Glut1 flox/+ conditional heterozygous mice, respectively. Male and female mice were used in all experiments.

CSF and blood glucose measurements

CSF was extracted from the cisterna magna using a protocol described by Pegg et al.[53]. Mice were anesthetized by intraperitoneal injection of pentobarbital (34.5-51.8 mg/kg), which was chosen to minimize increases in blood glucose levels, and secured in the prone position. The head was tilted forward at an angle of approximately 25 degrees. Using a sterilized scalpel, the skin was incised, and the muscle layers were carefully separated to provide access to the cisterna magna, located between the occipital bone and the first cervical vertebra. Cerebrospinal fluid (CSF) was collected from the cisterna magna using sterilized glass capillaries (1B150F-4, World Precision Instruments) connected to a winged needle and syringe assembly. Samples contaminated with blood were discarded. The glucose concentration in the collected CSF was measured using a blood glucose meter (Abbott Laboratories).

Simultaneously with the CSF collection, blood was sampled from the tail tip. While the mouse was secured in a stereotaxic frame, a small incision was made at the tip of the tail using a razor blade, and 2–3 μl of blood was collected. The blood glucose level was immediately measured using a blood glucose meter (Abbott Laboratories).

Measurement of glucose uptake into brain parenchyma.

Extracellular glucose levels were measured using a commercially available in vivo biosensor recording system (Pinnacle Technology) according to the manufacturer's instructions. A guide cannula was stereotaxically implanted to target the thalamus (AP −1.5 mm, ML −1.3 mm, DV −2.0 mm), and mice were allowed to recover for 1 week. Immediately before each recording, the glucose biosensor (standard mouse sensor) was calibrated using known glucose concentrations following the manufacturer's protocol, and then inserted into the guide cannula. Recordings were initiated after the signal stabilized; mice were additionally allowed to equilibrate for 1 h after sensor insertion to ensure a stable baseline. Glucose (0.03 g per mouse) was administered by oral gavage, and extracellular glucose was continuously recorded at 1 Hz. Signals were transmitted from the potentiostat to a computer and acquired using Sirenia Acquisition Software (Pinnacle Technology). Glucose elevation was quantified as the difference between the baseline level immediately before gavage and the peak level observed after gavage. The glucose response was quantified as the peak ΔISF glucose (peak value minus the mean baseline value immediately before gavage).

Behavioral tests

Prior to each behavioral test, mice were acclimated to the behavioral testing room for at least 30 minutes. The object location test (OLT) and novel object recognition test (NORT) were performed to assess memory function[54], while motor function was evaluated using the slip test[55].

Both the OLT and NORT consisted of three sessions: habituation, learning, and test. Mice were first placed in the center of the test apparatus (33 × 50 × 40 cm) and allowed to explore freely for 10 minutes, followed by a 1–2 hour return to their home cage. During the familiarization session, two identical objects (A and B) were placed in adjacent corners, 5 cm from the walls of the arena. Mice were reintroduced to the arena for 5 minutes, then returned to their home cage for 5 minutes. For the OLT test session, object B was moved to a diagonally opposite corner (designated B'), and mice were allowed to explore the arena for an additional 5 minutes. NORT was conducted immediately afterward. Mice were returned to the home cage for 5 minutes, and object A was replaced with a novel object (object C) in the same location. Mice were then placed back in the arena for another 5-minute test session.

Exploration times for objects A, B', and C were recorded to calculate the discrimination indices as follows:

- OLT = (B' − A) / (B' + A)
- NORT = (C − B') / (C + B')
- where A, B', and C represent the time spent exploring each object.

All behavioral tests were conducted under ambient lighting conditions of 10–15 lux. Mouse behavior was recorded using a ceiling-mounted charge-coupled device (CCD) camera positioned above the apparatus.

For the slip test, mice traversed a horizontal grid while being monitored with a side-mounted CCD camera. The number of times the hindlimb and forelimb falling through the grid was counted over 50 steps.

Immunohistochemistry of mice brain tissue

Following transcardial perfusion with phosphate-buffered saline (PBS) and 4% paraformaldehyde (PFA), whole brains were extracted, post-fixed overnight at 4 °C, and cryoprotected in 20% sucrose at 4 °C for one week. Serial coronal sections (50 μm thick) were prepared using a cryostat (CM3050 S; Leica Microsystems). Antigen retrieval was performed by incubating the sections in HistoVT One solution (Nacalai Tesque) at 70 °C for 30 minutes in a water bath. Sections were then permeabilized with a solution containing 0.2% Triton X-100, 1% Block Ace (DS Pharma Biomedical) in PBS for 30 minutes at room temperature. This was followed by overnight incubation with primary antibodies in PBS containing 0.4% Block Ace at room temperature. The immunostaining protocol continued with three washes in PBST (PBS with 0.05% Tween 20), followed by a 3-hour incubation with fluorophore-conjugated secondary antibodies diluted in PBS containing 0.4% Block Ace and 0.05% sodium azide. Nuclei were counterstained with 4′,6-diamidino-2-phenylindole (DAPI; Nacalai Tesque). Sections were subsequently washed three times in PBST, mounted in Fluoromount (Diagnostic BioSystems), and imaged using a FluoView FV3000 confocal laser scanning microscope (Olympus/Evident).

The following primary antibodies were used: goat anti-RFP (1:2000; Rockland, 200-101-379), guinea pig anti-Glut1 (1:1000; Frontier Institute, Af610), and/or rabbit anti-Sox9 (1:1000; Abcam, ab185966). Corresponding secondary antibodies included donkey anti-goat IgG conjugated to Cy™3 (1:1000; Jackson ImmunoResearch, 705-165-147), donkey anti-guinea pig IgG conjugated to biotin (1:1000; Jackson ImmunoResearch, 706-066-148), and/or donkey anti-rabbit IgG conjugated to Alexa™647 (1:1000; Jackson ImmunoResearch, 711-606-152). Tomato lectin (1:1000; Vector Laboratories, FL-1171) was used for vascular endothelial staining.

For enhanced immunostaining using horseradish peroxidase (HRP), endogenous peroxidase activity was quenched by incubating sections in 1% H_2O_2 in PBS for 20 minutes after antigen retrieval, followed by PBS washes. The standard immunostaining protocol was then followed. After the secondary antibody incubation and subsequent washes, sections were incubated with the avidin–biotin–peroxidase complex using the VECTASTAIN Elite ABC Kit (Vector Laboratories, PK-6100) for 30 minutes and washed three times with PBST. HRP activity was visualized using Tyramide Signal Amplification (TSA) with Cyanine5 (1:500; PerkinElmer, FP1171).

In Fig. 1, Aldh1l1-CreERT2; tdTomato reporter mice were administered tamoxifen intraperitoneally at 100 mg/kg once daily for three consecutive days starting at P45. Brains were fixed and processed for immunostaining analysis three weeks after the final tamoxifen injection.

Plasmid construction for AAV production

The AAV expression vector, pAAV-CAG-hGLUT1-MycTag-T2A-mCherry-WPRE, was constructed by custom DNA synthesis (VectorBuilder). The hGLUT1 coding sequence corresponds to NM_006516.4.

AAV Production and Purification

pAAV-BR1 was artificially synthesized by inserting the 7-amino acid peptide NRGTEWD between positions 588 and 589 of the AAV2 capsid[36], along with an N587Q substitution (asparagine to glutamine). Similarly, pAAV-X1.1 was generated by inserting the 7-amino acid peptide DGAATKN between positions 588 and 589 of the AAV9 capsid[37,56]. The production of pAAV-AST is described in results.

HEK293T cells were cultured in standard medium (D-MEM supplemented with 10% heat-inactivated fetal bovine serum [hiFBS] and 1% penicillin–streptomycin [PS]) until reaching approximately 90% confluency. The cells were triple-transfected using polyethylenimine (PEI-Max) to produce AAV vectors, following the protocol described by Grieger et al[57]. (2006). Briefly, the transgene expression plasmid (pAAV-CAG-hGLUT1-MycTag-T2A-mCherry-WPRE), a packaging plasmid (pAAV-AST, pAAV-BR1, or pAAV-X1.1), and the pHelper plasmid were diluted and mixed in Opti-MEM (Life Technologies) to allow for the formation of DNA-PEI complexes.

Six to twelve hours after transfection, the culture medium was replaced with D-MEM containing 2% hiFBS and 1% PS. Viral particles were harvested from the medium 7–10 days post-transfection. For viral recovery, the collected supernatant was mixed with a 5× AAV precipitation buffer (200 g PEG 8000 [Sigma-Aldrich] and 73.05 g NaCl in 500 mL H_2O) and incubated at 4 °C for 2–3 hours, as described by Guo et al[58]. The mixture was then centrifuged at 3,000 × g for 30 minutes at 4 °C. The resulting PEG precipitate was resuspended in Dulbecco's PBS (D-PBS) and treated with SuperNuclease (Sino Biological) in the presence of 5 mM MgCl2 for 60 minutes to digest residual host cell DNA and RNA. The reaction was subsequently terminated by the addition of 6.5 mM EDTA.

Finally, the virus was purified using an iodixanol discontinuous gradient, as described by Zolotukhin et al[59]. Briefly, following centrifugation to remove cellular debris, the clarified supernatant was layered onto an iodixanol (OptiPrep) step gradient (15%, 25%, 40%, and 54%) in an Ultra-Clear tube (25 × 89 mm; Beckman). The gradient was ultracentrifuged at 28,000 rpm for 18 hours at 10 °C. Viral fractions were then collected from the bottom three-fourths of the 40% layer to the top one-fourth of the 54% layer (approximately 4–5 mL) using a 19G needle. The eluate was buffer-exchanged and concentrated from PBS to HBSS using a Vivaspin 100K centrifugal filter (Sartorius).

AAV purity was evaluated by SDS-PAGE, and viral genome titers were quantified by qPCR using the KAPA SYBR Fast qPCR Kit (Nippon Genetics). Primers targeting the WPRE sequence were used:

- Forward: 5′-CTGTTGGGCACTGACAATTC-3′
- Reverse: 5′-GAAGGGACGTAGCAGAAGGA-3′

The expression plasmid served as the standard for quantification.

Peptide motif analysis

Selection of analyzed datasets: Four published AAV insertion library studies were analyzed. [30-33]. From Kumar et al., motifs showing $\log_{10}$ enrichment > 1 in GFAP-positive cells were extracted, clustered to remove near-identical variants, and representative sequences were selected. Together with five motifs from Nonnenmacher and one each from Kunze and Hanlon, these comprised 15 reference motifs forming the analytical dataset. Extraction and scoring: Flanking residues derived from the VP3 587–590 loop (A–Q/A–Q) were trimmed, retaining only the 7-residue insertions between VP3 588–589 (pos1–pos7). The 15 normalized sequences were aligned to construct a position-frequency matrix (PFM). For each candidate sequence, a relative logo score was calculated as the product of residue probabilities at each position, normalized to the highest score (= 1.0): Relative logo score(seq) = $[\Pi(i=1\rightarrow7)\ (n_i,aa / N)] / \max[\Pi(i=1\rightarrow7)\ (n_i,aa / N)]$ where n_i,aa is the frequency of residue aa at position i and N is the total number of reference motifs. Sequence logos were generated from the position-frequency matrix using a custom Python/Matplotlib script. Empirical validation threshold (≥ 0.8): Across datasets, astrocyte-tropic motifs reported by Kumar and Nonnenmacher consistently exhibited relative logo scores ≥ 0.8, retaining the consensus T(L/A/T)xxPF[K/L]. Motifs scoring ≥ 0.9 were nearly identical to PHP.eB-derived variants, whereas those 0.8–0.89 preserved the consensus with limited substitutions. Motifs below 0.8 showed partial loss of the PF core and rarely yielded robust astrocyte expression; therefore, 0.8 was adopted as the empirical cutoff for validation.

***In vivo* administration of AAV-AST0, AAV-AST and AAV-AST3 in wild-type mice**

C57BL/6J mice at postnatal day 18 (P18) or 3 months of age received retro-orbital injections of AAV-AST0, AAV-AST, or AAV-AST3 at 3 × 10^11 viral genomes (vg) per mouse.

Cell Culture

Human brain microvascular endothelial cells (hBMECs; ACBRI 376) and the specialized complete medium kit with serum and CultureBoost (4Z0-500-R) were purchased from Cell Systems. Human cortical astrocytes (HAs; 1800) and Astrocyte Medium (AM; Cat. #1801) were obtained from ScienCell Research Laboratories. All cells were maintained at 37°C in a humidified atmosphere containing 5% CO_2.

Plasmid Construction

Reporter plasmids featuring promoter/enhancer fusions with the *mCherry* gene were designed for subsequent recombinant adeno-associated virus (rAAV) production. To this end, each expression cassette was flanked by inverted terminal repeat (ITR) sequences, and

a Woodchuck Hepatitis Virus Posttranscriptional Regulatory Element (WPRE) was incorporated to enhance transgene expression. Specifically, candidate cis-regulatory regions (Regions a–i) were selected as promoter/enhancer regions from the human SLC2A1 gene locus (Chr1: 42,956,501–42,968,500, GRCh38/hg38). These fragments were amplified by PCR using human genomic DNA extracted from the HEK293 cell line as a template. To construct the reporter vectors, the pAAV-CAG-mCherry plasmid was digested with *Xba*I and *Xho*I to obtain a linear backbone containing the *mCherry*, WPRE, and ITR sequences. Finally, the linear vector and the respective promoter/enhancer fragments were assembled using NEBuilder® HiFi DNA Assembly Master Mix (New England Biolabs, Cat. #E2621), placing the regulatory elements upstream of the *mCherry* gene within the ITRs. The resulting plasmids were transformed into *Escherichia coli* (*E. coli*) DH5α competent cells (Takara Bio, Cat. #9057) and purified using NucleoBond Xtra Midi (Takara Bio, Cat. #740410). A plasmid expressing GFP under the CAG promoter was used as an internal control.

Transfection and Immunostaining

hBMECs or HAs were seeded at a density of 10,000 cells/well in 24-well plates 24 hours prior to transfection. In each well, 0.25 μg of the pAAV-hSLC2A1p-mCherry vector and 0.25 μg of the pAAV-CAG-GFP control vector were co-transfected using Lipofectamine LTX (Thermo Fisher Scientific, Cat. #15338100) according to the manufacturer's protocol. The negative control received no treatment. After 48 hours, cells were fixed with 4% paraformaldehyde. To enhance the sensitivity of fluorescent protein detection, an anti-RFP antibody (Rockland, Cat. #200-101-379) and an anti-GFP antibody (Abcam, Cat. #ab13970) were used as primary antibodies. For fluorescence microscopy, RFP (mCherry) was targeted with Cy3-conjugated secondary antibodies, and GFP was detected using Alexa Fluor 488-conjugated secondary antibodies. Subsequently, nuclei were counterstained with DAPI to visualize cellular architecture.

Imaging and Statistical Analysis

Fluorescence observation and quantitative analysis were performed using an FV3000 confocal laser scanning microscope, with all images captured under identical laser power and detection settings across all samples. For quantification, images captured with a Keyence BZ-X1000 microscope were analyzed using ImageJ software (NIH). Reporter activity was defined as the percentage of mCherry-positive cells exceeding a fixed fluorescence intensity threshold among the total GFP-positive cell population. Quantification was performed using 15 fields per condition from 3 independent experiments; field-level measurements were averaged within each experiment, and n represents independent experiments.

Administration of AAVs for Glut1 del/+ mice

AAVs were administered via the retro-orbital sinus[60] to Glut1 del/+ mice between P15 and P19. Mice were anesthetized using a combination of three agents: medetomidine (0.375 mg/kg; Nippon Zenyaku Kogyo Co., Ltd., Fukushima, Japan), midazolam (2 mg/kg; Maruishi Pharmaceutical Co., Ltd., Osaka, Japan), and butorphanol (2.5 mg/kg; Meiji Seika Pharma

Co., Ltd., Tokyo, Japan). Glut1 del/+ mice received AAV-BR1, AAV-X1.1 and/or AAV-AST at doses of 1.0–7.5 × 10^{11} vg per mouse for each virus, diluted in 100 μL of Hanks' Balanced Salt Solution (HBSS) containing 0.5% Fast Green. Control littermates received 100 μL of vehicle (HBSS with 0.5% Fast Green) via the same retro-orbital injection method.

Statistics

Statistical analyses are described in the figure legends. All analyses were performed using GraphPad Prism 10 (GraphPad Software). The number of animals used for each experiment/analysis can be found in each figure legend.

Data availability statement

All data supporting the findings of this study are available within the paper and its supplementary information files. Additional data are available from the corresponding author upon reasonable request.

Acknowledgments

We thank Dr. T. Hara (TMiMS, Tokyo, Japan) for kindly sharing Tie2-Cre mice. We are also grateful to Dr. M. Murakami (The University of Tokyo, Tokyo, Japan) for generously providing CAG-Cre mice, originally generated by Dr. J. Miyazaki (Osaka University, Suita, Japan). We further thank Dr. M. Hasegawa (TMiMS, Tokyo, Japan) and Dr. A. Nagakura (Tokyo Metropolitan Matsuzawa Hospital, Tokyo, Japan) for coordinating the acquisition and distribution of postmortem brain samples. Finally, we express our deepest gratitude to the families of the deceased individuals for their generous donation of brain tissue and for their time and cooperation during the consent and interview process.

Funding

This work was supported by the JST FOREST Program (JPMJFR2169 to S.H.);
the Food Science Institute Foundation (Ryoushoku-kenkyukai);
the Takeda Science Foundation;
the Naito Foundation (to S.H.); and
the Ichiro Kanehara Foundation (to S.T.).

Author contributions

S.H. designed the study. S.T., H.S., N.A., E.S., K.S. and S.H. performed experiments. S.T. and S.H. performed data and image analysis. K.S. provided critical input on immunostaining of

postmortem brain. S.T. wrote the manuscript. H.O. and S.H. edited the manuscript. S.H. supervised this study.

Figure 1

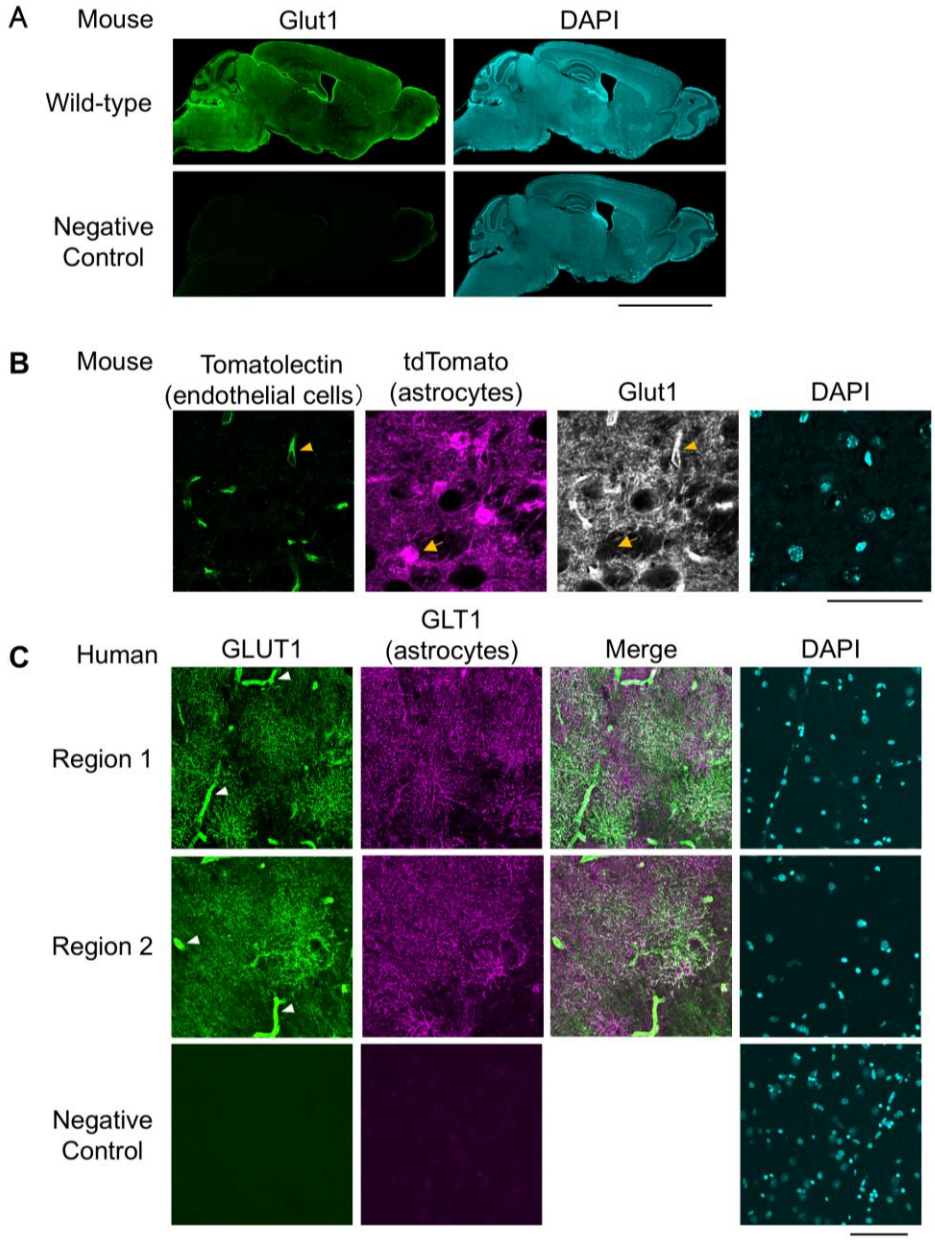
A
Mouse
Glut1
DAPI
Wild-type
Negative Control
B
Mouse
Tomatolectin (endothelial cells)
tdTomato (astrocytes)
Glut1
DAPI
C
Human
GLUT1
GLT1 (astrocytes)
Merge
DAPI
Region 1
Region 2
Negative Control

Figure 1. Glut1/GLUT1 expression in mouse and human brain.

(A) Representative sagittal brain sections from wild-type mice immunostained for Glut1 (green) and counterstained with DAPI (cyan). Negative control sections were processed in parallel without the primary anti-Glut1 antibody. Scale bar, 5 mm.(B) High-magnification images of the thalamic ventral posteromedial nucleus (VPM) from 2-month-old Aldh1l1-CreERT2; Rosa26^LSL-tdTomato (flex tdTomato) mice. Endothelial cells were labeled with tomato lectin (green), astrocytes with tdTomato (magenta), Glut1 immunoreactivity is shown in grayscale, and nuclei are counterstained with DAPI (cyan). Yellow arrowheads indicate Glut1 signal associated with lectin-positive vessels, and yellow arrows indicate Glut1 signal in tdTomato-positive astrocyte somata. Scale bar, 50 μm. (C) Representative images from normal human hippocampus stained for GLUT1 (green) and the astrocytic marker GLT1 (magenta), with merged images and DAPI (cyan). White arrowheads indicate vascular GLUT1 staining. Region 1 and Region 2 correspond to the stratum oriens (or alveus) and the pyramidal cell layer, respectively. Negative control sections were processed without primary antibodies. Scale bar, 50 μm. Glut1/GLUT1 immunostaining was visualized using tyramide signal amplification (TSA).

Figure2

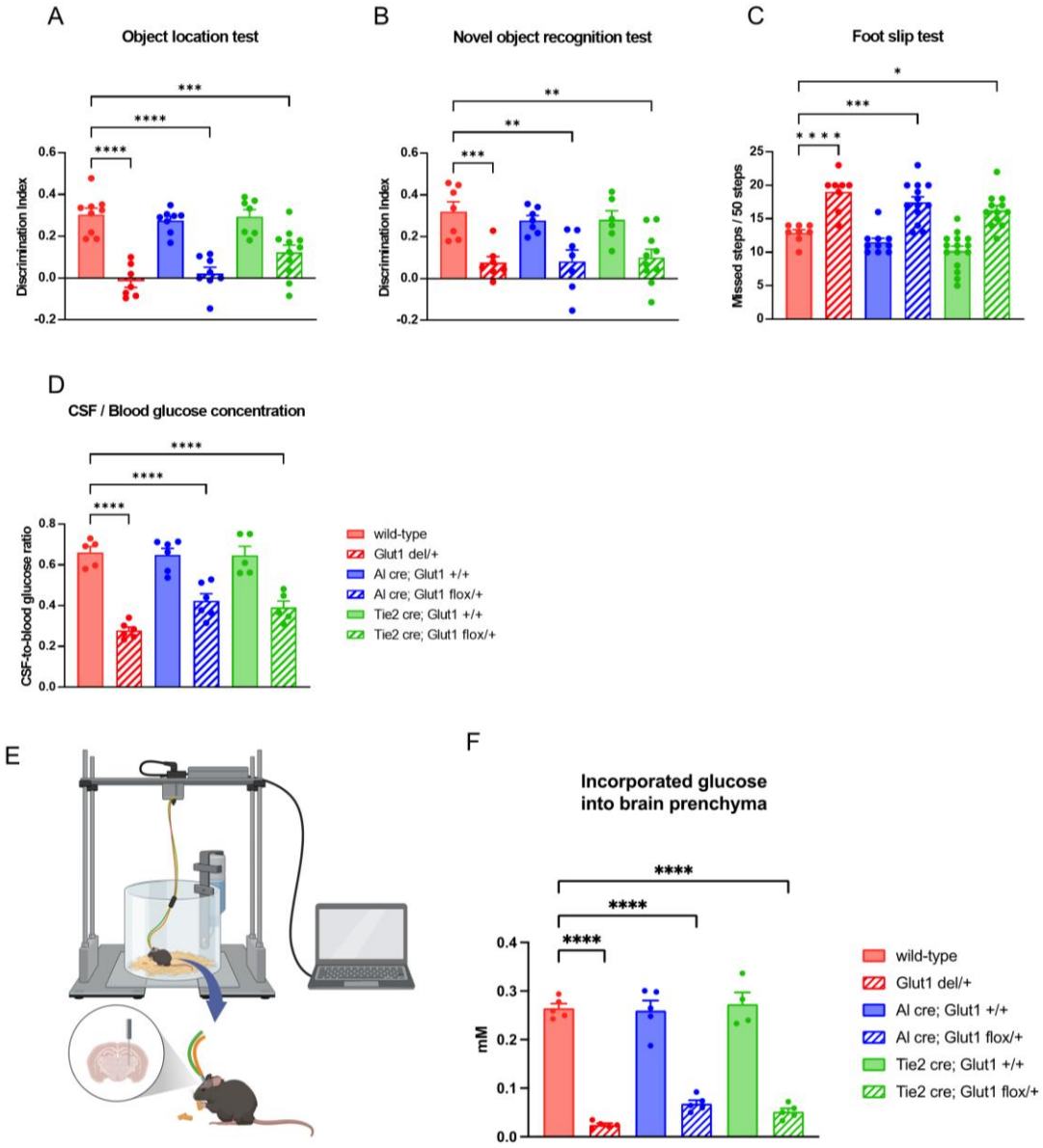
A
Object location test
Discrimination Index
B
Novel object recognition test
Discrimination Index
C
Foot slip test
Missed steps / 50 steps
D
CSF / Blood glucose concentration
CSF-to-blood glucose ratio
wild-type
Glut1 del/+
Al cre; Glut1 +/+
Al cre; Glut1 flox/+
Tie2 cre; Glut1 +/+
Tie2 cre; Glut1 flox/+
E
F
Incorporated glucose
into brain prenchyma
mM
wild-type
Glut1 del/+
Al cre; Glut1 +/+
Al cre; Glut1 flox/+
Tie2 cre; Glut1 +/+
Tie2 cre; Glut1 flox/+

Figure 2. Astrocyte- and endothelial-specific Glut1 haploinsufficiency recapitulates key features of GLUT1 deficiency syndrome.

(A–C) Behavioral analyses in six groups: wild-type, systemic Glut1 del/+ mice, Aldh1l1-Cre (Al cre); Glut1 +/+ mice, Al cre; Glut1 flox/+ mice, Tie2-Cre; Glut1 +/+ mice, and Tie2-Cre; Glut1 flox/+ mice (n = 6–15 mice per group). (A) Object location test (OLT) and (B) novel object recognition test (NORT) were used to assess spatial and recognition memory (discrimination index). (C) The foot-slip test evaluated motor coordination (missed steps per 50 steps). (D) CSF-to-blood glucose ratio measured in the same cohorts (n = 5–6 mice per group). Blood glucose levels were comparable across groups (see Supplementary Fig. 1). (E) Schematic of the *in vivo* recording setup for thalamic interstitial fluid (ISF) glucose measurement. Illustration created with BioRender. (F) ISF glucose measured following oral glucose administration (0.03 g per mouse, gavage). The increase in ISF glucose was markedly blunted in systemic, astrocyte-specific, and endothelial-specific Glut1 haploinsufficient mice compared with wild-type controls (n = 4–5 mice per group). Data are presented as mean ± SEM; dots represent individual mice. Statistical significance was determined by one-way ANOVA followed by Dunnett's multiple-comparison test (*$p < 0.05$, **$p < 0.01$, ***$p < 0.001$, ****$p < 0.0001$).

Figure 3

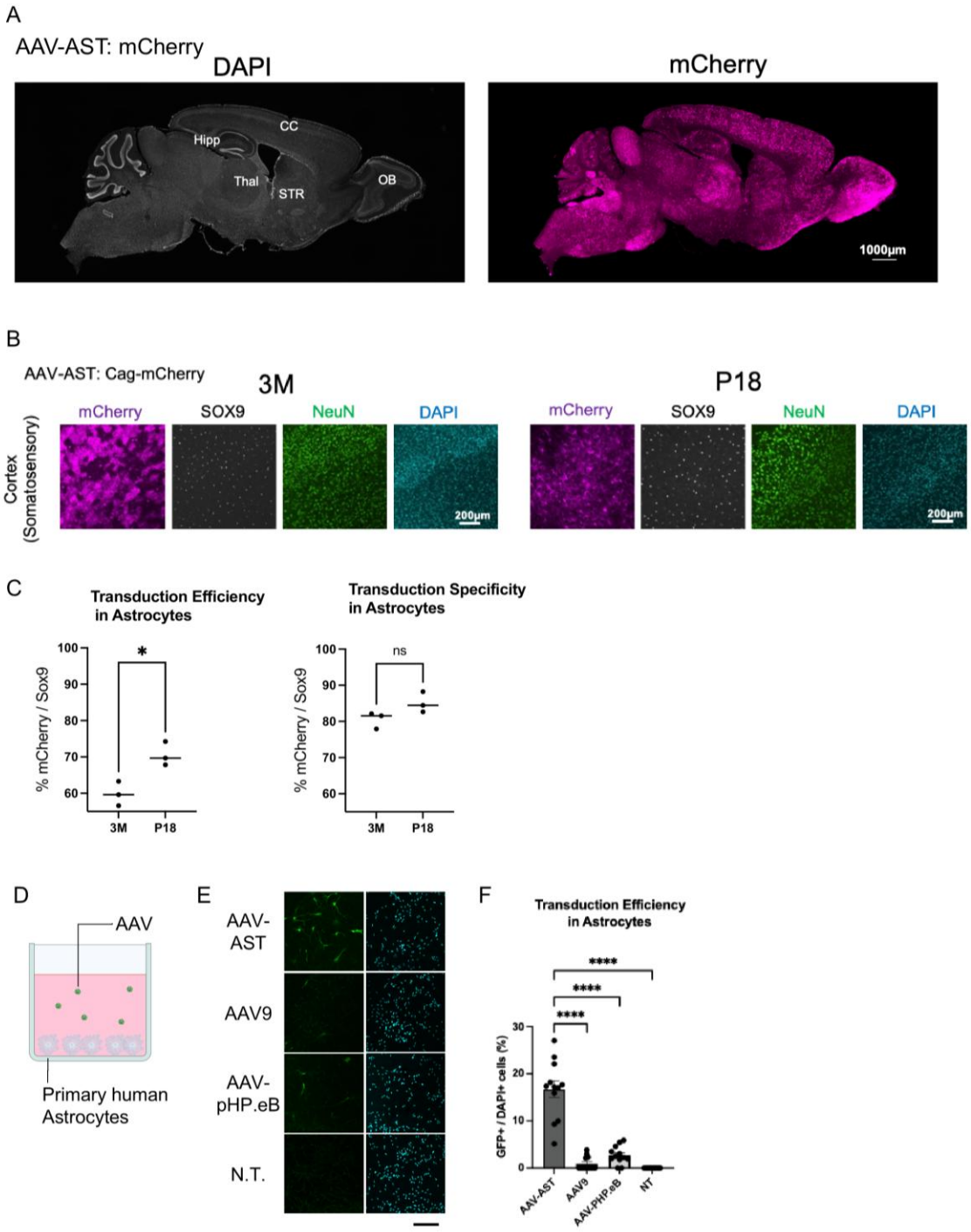
A
AAV-AST: mCherry
DAPI
mCherry
CC
Hipp
Thal
STR
OB
1000µm
B
AAV-AST: Cag-mCherry
3M
P18
mCherry
SOX9
NeuN
DAPI
Cortex (Somatosensory)
200µm
C
Transduction Efficiency in Astrocytes
Transduction Specificity in Astrocytes
% mCherry / Sox9
*
ns
3M
P18
D
AAV
Primary human Astrocytes
E
AAV-AST
AAV9
AAV-pHP.eB
N.T.
F
Transduction Efficiency in Astrocytes
GFP+ / DAPI+ cells (%)
****
AAV-AST
AAV9
AAV-PHP.eB
NT

Figure 3. Astrocyte-selective transduction of AAV-AST *in vivo* and *in vitro*.

(A) Representative sagittal brain sections showing mCherry expression (magenta) after retro-orbital administration of AAV-AST–CAG-mCherry into adult mice (3 months; 100 μL, 3.3 × 10^11 vector genomes (vg) per mouse). DAPI is shown in gray. Labeled regions: OB, olfactory bulb; CC, cerebral cortex; Thal, thalamus; STR, striatum; Hipp, hippocampus. Scale bar, 1,000 μm. (B) Representative immunofluorescence images of the somatosensory cortex 3 weeks after AAV administration at postnatal day 18 (P18) or 3 months (3M). mCherry (magenta), SOX9 (astrocytes, gray), NeuN (neurons, green), and DAPI (nuclei, cyan). Scale bar, 200 μm. (C) Quantification of astrocyte transduction efficiency (left; % of SOX9^+ cells expressing mCherry) and astrocyte specificity (right; % of mCherry^+ cells that are SOX9^+). Data are mean ± SEM (n = 3 mice per group). Two-sided Welch's t-test; *p < 0.05; ns, not significant. (D) Schematic of the in vitro astrocyte transduction assay using AAVs packaging a CAG-driven GFP reporter (CAG-GFP). Primary human astrocytes were cultured in monoculture, transduced with AAVs, and fixed 3 days later for fluorescence imaging. Created with BioRender.com. (E) Representative fluorescence images of astrocytes transduced with the indicated AAVs (GFP, green; DAPI, cyan). NT, non-transduced control. Scale bar, 200 μm. (F) Quantification of astrocyte transduction efficiency corresponding to (E) (GFP^+/DAPI^+ cells, %). Data are mean ± SEM. Statistical significance was determined by one-way ANOVA followed by Tukey's multiple-comparison test (****p < 0.0001).

Figure 4

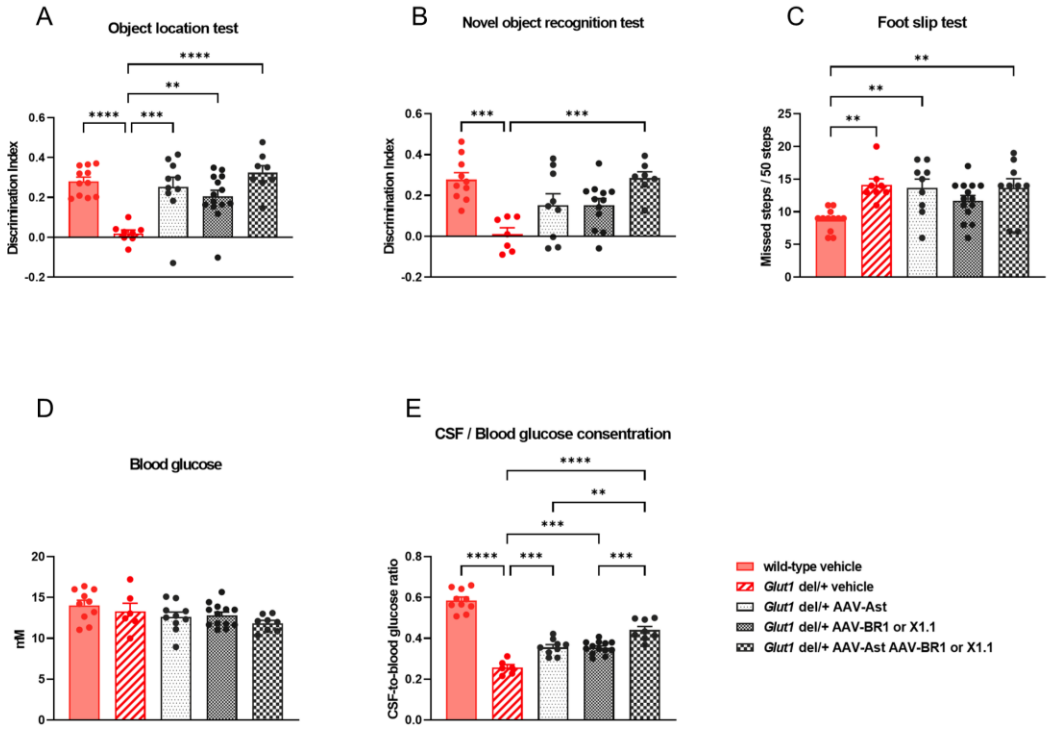

Figure 4. Cell-type–targeted AAV-Glut1 supplementation differentially rescues GLUT1-DS–like phenotypes.

(A–C) Behavioral analyses in five groups: wild-type + vehicle, Glut1 del/+ + vehicle, Glut1 del/+ + AAV-AST–Glut1 (astrocyte-targeted), Glut1 del/+ + AAV-BR1 (or X1.1)–Glut1 (endothelial-targeted), and Glut1 del/+ + AAV-AST–Glut1 + AAV-BR1(or X1.1) –Glut1. AAVs were administered between postnatal days 15 and 19 (P15–P19) via retro-orbital injection, and behavioral testing was performed starting at P48 (n = 5–14 mice per group). (A) Object location test (OLT) and (B) novel object recognition test (NORT) were used to assess memory performance (discrimination index). (C) Foot-slip test evaluated motor coordination (missed steps per 50 steps). (D,E) Blood glucose concentration (D) and CSF-to-blood glucose ratio (E) were measured (n = 6–14 mice per group). Data are presented as mean ± SEM; dots represent individual mice. Statistical significance was determined by one-way ANOVA followed by Tukey's multiple-comparisons test (****$p < 0.0001$, ***$p < 0.001$, **$p < 0.01$, *$p < 0.05$).

Figure 5

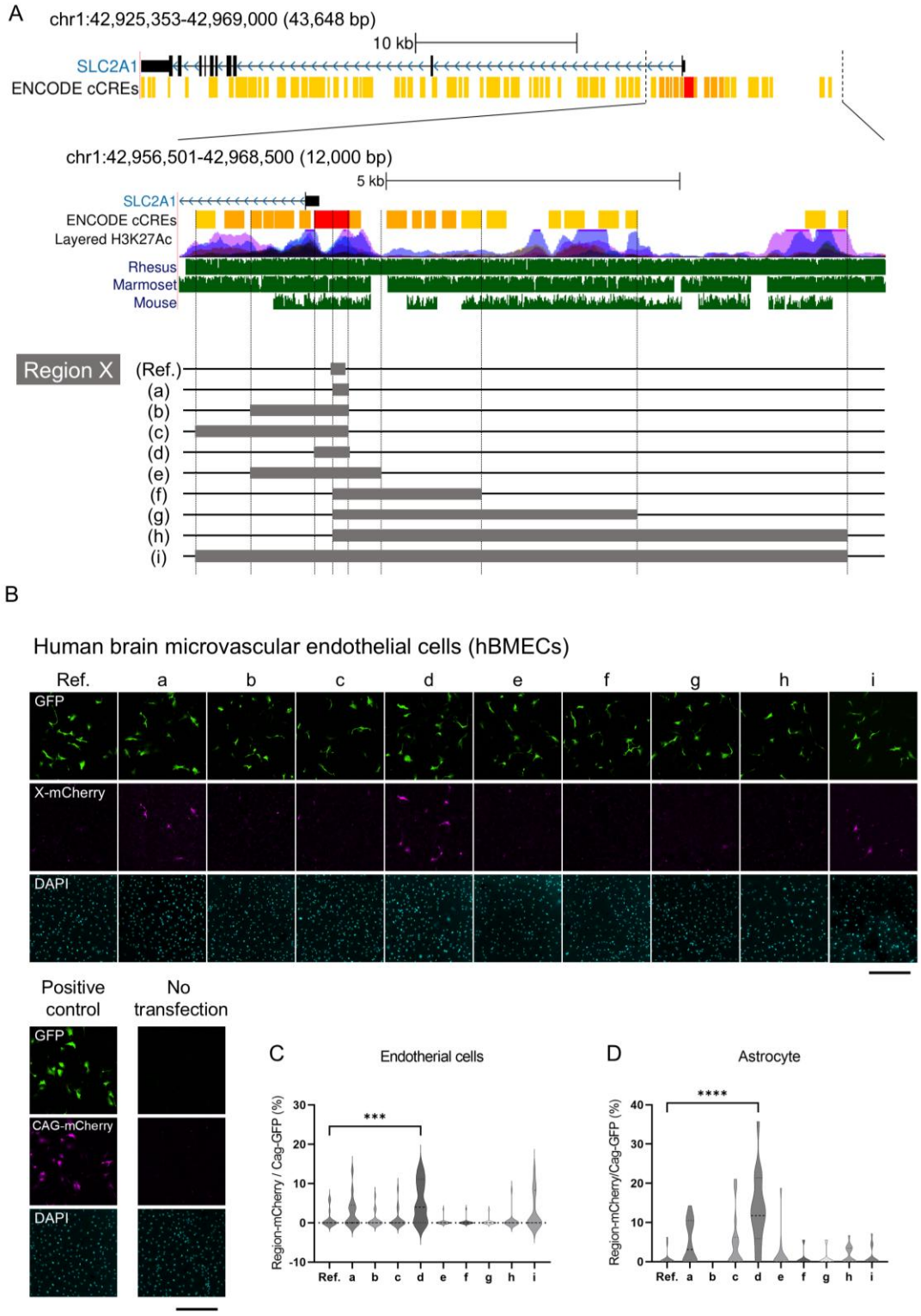
A
chr1:42,925,353-42,969,000 (43,648 bp)
10 kb
SLC2A1
ENCODE cCREs
chr1:42,956,501-42,968,500 (12,000 bp)
5 kb
SLC2A1
ENCODE cCREs
Layered H3K27Ac
Rhesus
Marmoset
Mouse
Region X
(Ref.)
(a)
(b)
(c)
(d)
(e)
(f)
(g)
(h)
(i)
B
Human brain microvascular endothelial cells (hBMECs)
Ref.
a
b
c
d
e
f
g
h
i
GFP
X-mCherry
DAPI
Positive control
No transfection
GFP
CAG-mCherry
DAPI
C
Endotherial cells
Region-mCherry / Cag-GFP (%)
***
D
Astrocyte
Region-mCherry/Cag-GFP (%)
****

Figure 5. Functional validation of predicted cis-regulatory regions at the human SLC2A1 locus.

(A) UCSC Genome Browser view of the human *SLC2A1* locus (GRCh38/hg38) showing ENCODE candidate cis-regulatory elements (cCREs; orange), layered H3K27ac enrichment (purple), and sequence conservation across rhesus, marmoset, and mouse (green). Gray boxes indicate predicted regulatory fragments (Ref. and Regions a–i) selected for functional testing and cloned upstream of an mCherry reporter (RegionX-mCherry). (B) Representative images of human brain microvascular endothelial cells (hBMECs) transfected with each RegionX-mCherry reporter (magenta) together with a CAG-GFP transfection control (green); nuclei were counterstained with DAPI (cyan). A CAG-mCherry plasmid served as a positive control for mCherry expression, and non-transfected cells served as a negative control. Scale bar, 300 μm. (C) Quantification of reporter activity in hBMECs, expressed as RegionX-mCherry/CAG-GFP (%) (n=3 independent experiments; 15 fields per experiment; violin plots with median and interquartile range (IQR; 25th–75th percentiles)). Statistical significance versus Ref. was assessed by one-way ANOVA followed by Dunnett's multiple-comparisons test (***$p < 0.001$). (D) Functional validation in primary cultured human astrocytes, performed as in (C). Reporter activity is shown as RegionX-mCherry/CAG-GFP (%) (n=3 independent experiments; 15 fields per experiment; violin plots with median and interquartile range (IQR; 25th–75th percentiles)). Statistical significance versus Ref. was assessed by one-way ANOVA followed by Dunnett's multiple-comparisons test (****$p < 0.0001$).

Figure 6

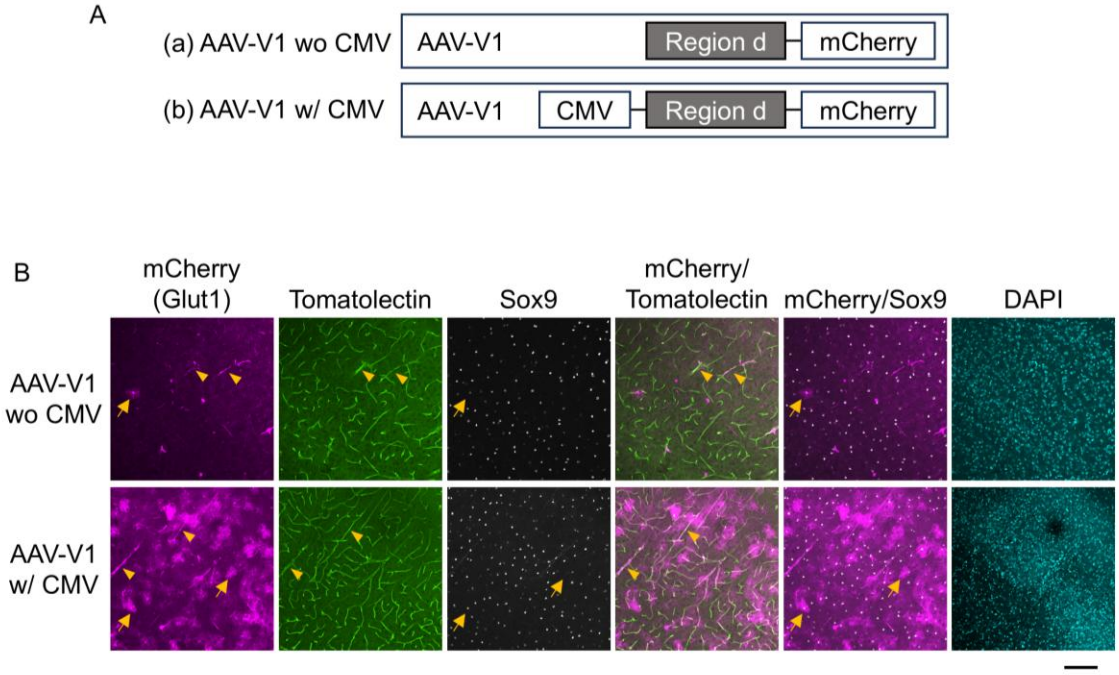

Figure 6. *In vivo* validation of Region d regulatory activity using AAV-V1.

(A) Reporter constructs containing Region d, with or without an upstream CMV enhancer element, were packaged into AAV-V1 capsids and administered to wild-type mice by retro-orbital injection. (B) Representative confocal images of cortical sections stained with lectin (vascular endothelial cells) and SOX9 (astrocytes). Top, AAV-V1 carrying Region d alone drove mCherry expression predominantly in vascular endothelial cells, with detectable expression in astrocytes. Bottom, addition of a CMV enhancer upstream of Region d increased reporter signal without an obvious change in cell-type distribution, resulting in a pattern that more closely recapitulates endogenous *SLC2A1* expression. Yellow arrowheads indicate representative vascular endothelial cells, and yellow arrows indicate astrocytes. Scale bar, 100 μm.

Supplementary Fig.1

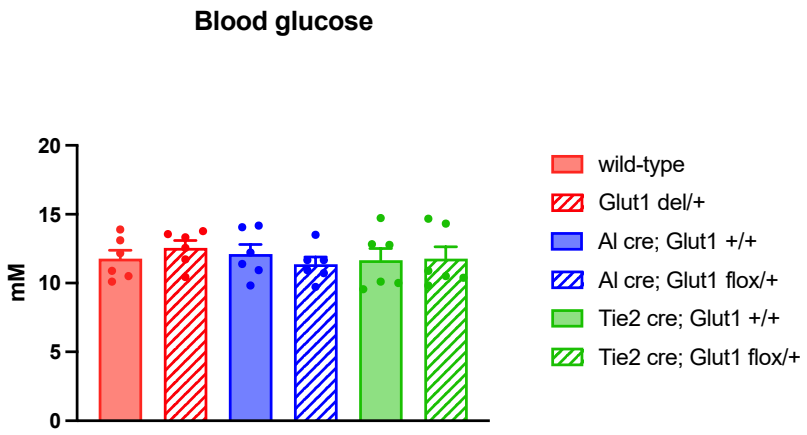

Supplementary Fig. 1 | Random-fed blood glucose in mice with cell type–specific Glut1 haploinsufficiency.

Random-fed (non-fasted) blood glucose concentrations in the indicated genotypes. Bars represent mean ± SEM (n = 6 mice per group). Statistical significance was assessed by one-way ANOVA followed by Tukey's multiple-comparisons test; no significant differences were observed among groups.

Supplementary Fig.2

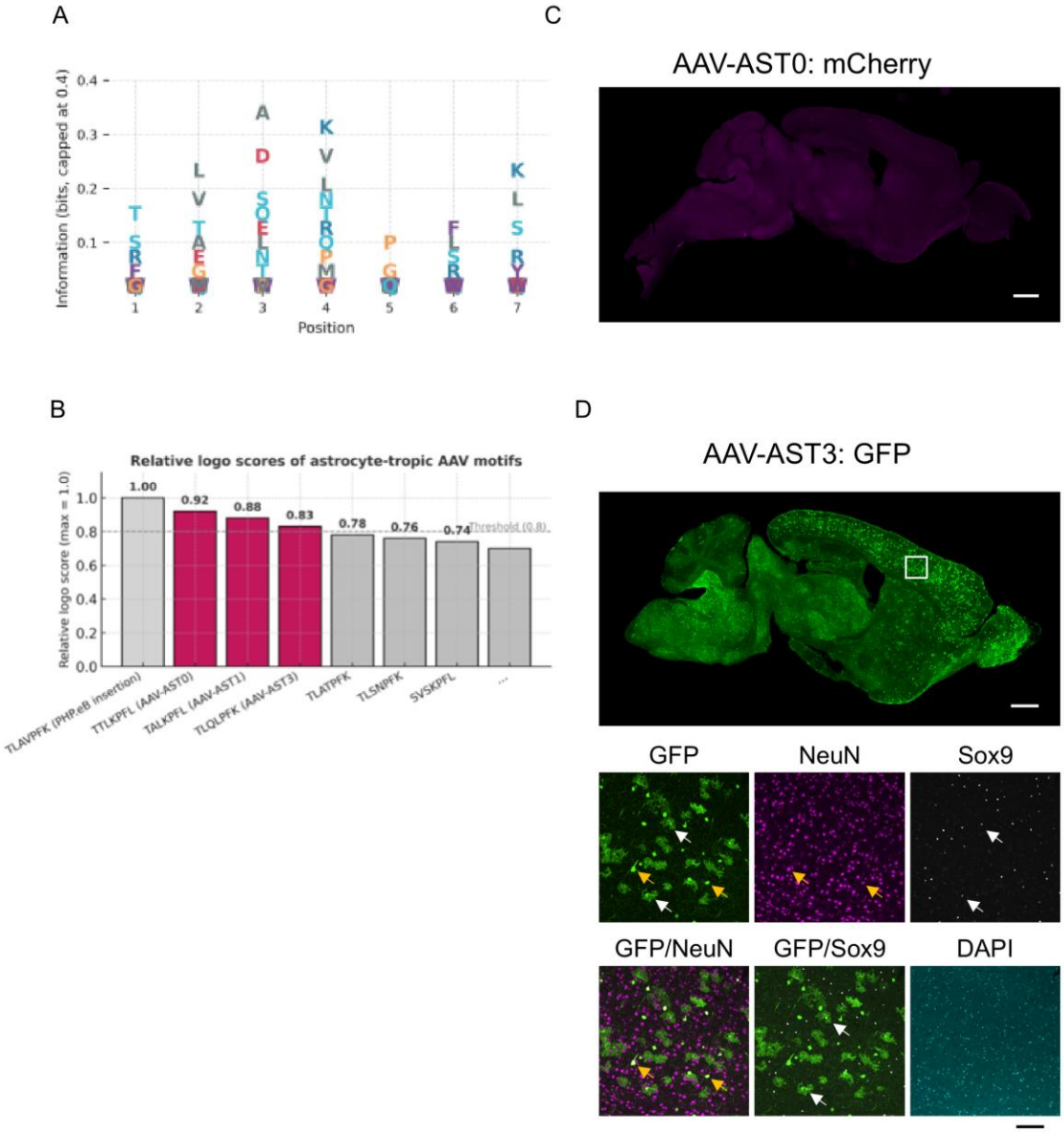

Supplementary Fig. 2 | Conserved motif structure and logo-score ranking of astrocyte-tropic AAV insertions.

(A) Sequence logo representing the heptapeptide consensus derived from the reference astrocyte-tropic motifs used to generate the position-frequency matrix (PFM). Strong conservation was observed at Thr (position 1) and Pro–Phe (positions 5–6), defining a T(L/A/T)xxPF(K/L) core motif characteristic of astrocyte-tropic variants. (B) Relative logo scores for the reference motifs used to build the PFM and for newly derived candidate motifs (AAV-AST0, AAV-AST1, and AAV-AST3), scored by applying the PFM. Scores are

normalized to the maximum (max = 1.0). Motifs with scores ≥ 0.8 are highlighted, indicating sequences prioritized for experimental validation. TLAVPFK (PHP.eB insertion; score = 1.00) was not prioritized because it is identical to the PHP.eB insertion. (C,D) Representative sagittal brain sections following intravenous administration (retro-orbital injection) of AAV-AST0:CAG-mCherry (C) and AAV-AST3:CAG-GFP (D) into 3-month-old mice (100 μL, 3.3 × 10^11 vg per mouse). Scale bars, 1,000 μm. Enlarged views in (D) show immunostaining for GFP together with NeuN and SOX9. White and yellow arrows indicate representative SOX9-positive astrocytes and NeuN-positive neurons colocalized with GFP signals, respectively. Scale bars, 100 μm.

Supplementary Fig. 3

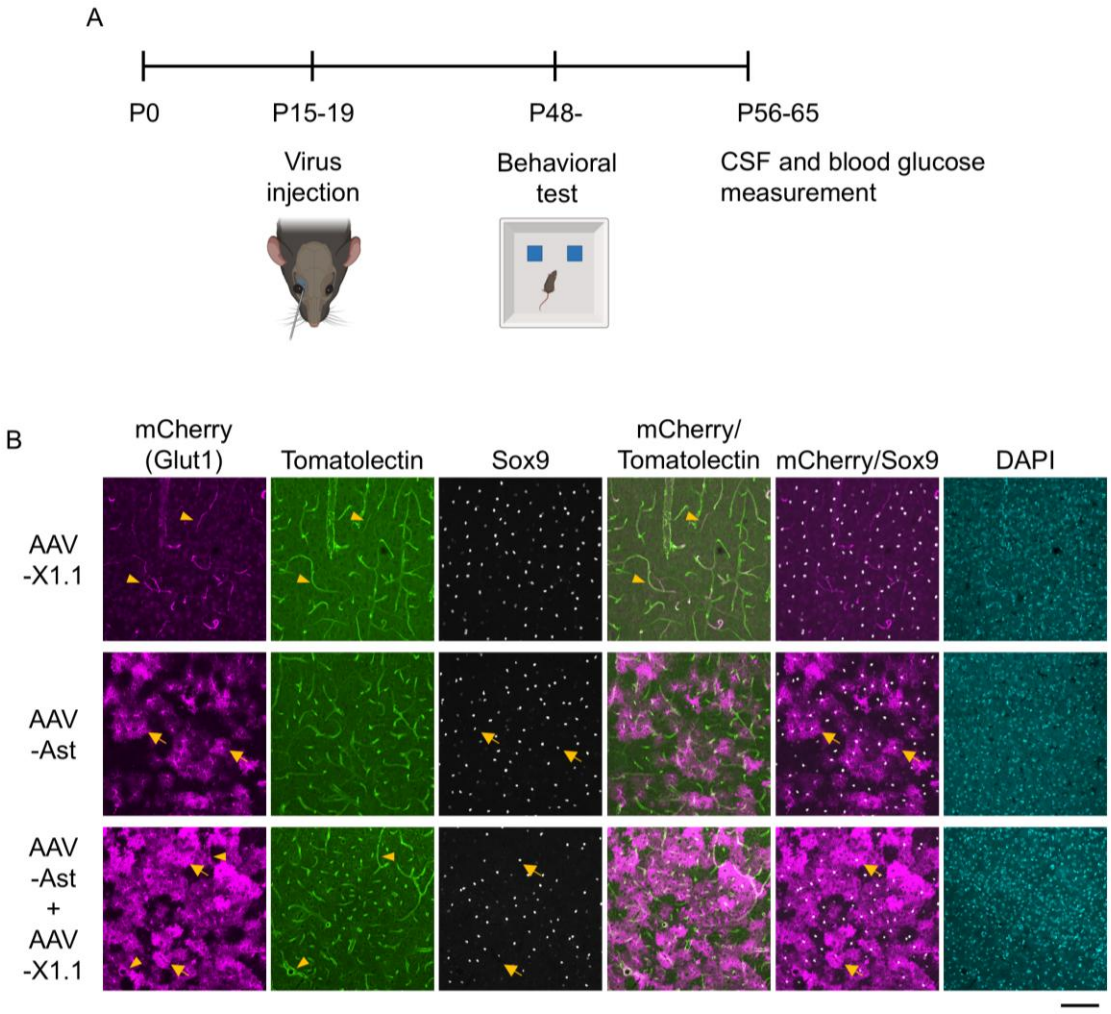

Supplementary Fig. 3 | Cell-type–specific Glut1 supplementation in Glut1 haploinsufficient mice via AAV administration.

(A) Experimental workflow for Glut1 supplementation using AAV. The illustration was created with BioRender. (B) Representative transgene expression after intravenous delivery of AAV-X1.1 (EC-targeting), AAV-AST (astrocyte-targeting), or AAV-AST + AAV-X1.1 (dual targeting) in Glut1 haploinsufficient mice. Representative confocal z-stack maximum-intensity projections were acquired from the cortex of Glut1 haploinsufficient mice injected with AAV. mCherry is shown in magenta, lectin in green, SOX9 in white, and DAPI in cyan. Yellow arrows and arrowheads indicate representative astrocytes and ECs colocalized with mCherry, respectively. Scale bar, 100 μm.

Supplementary Fig. 4

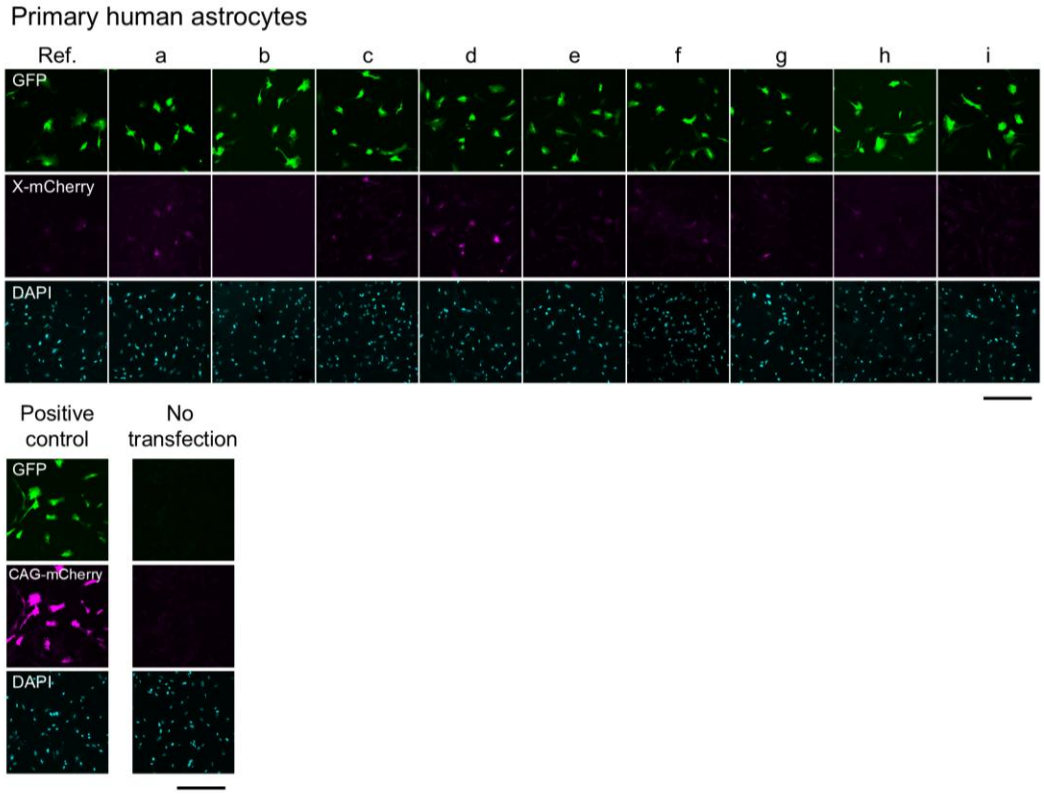

Supplementary Fig. 4 | Functional validation of human SLC2A1 regulatory regions in primary human astrocytes.

Reporter constructs containing candidate SLC2A1 regulatory regions (a–i) upstream of mCherry were transfected into primary cultured human astrocytes. CAG-GFP was co-transfected to monitor transfection efficiency in all conditions, except for the non-transfected negative control. As a positive control, CAG-mCherry was co-transfected with CAG-GFP. GFP is shown in green, mCherry in magenta, and DAPI in cyan. Scale bar, 300 μm.

Supplementary Fig. 5

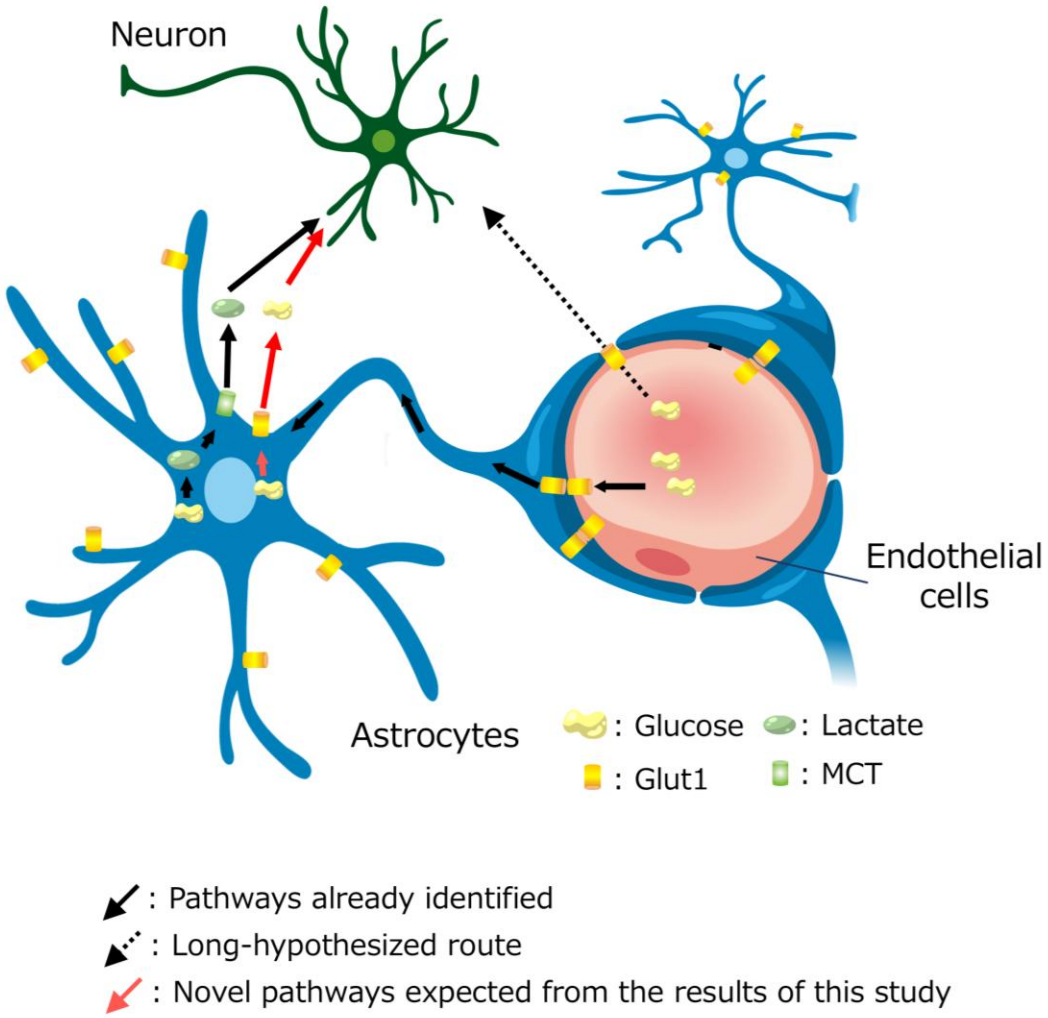

Supplementary Fig. 5 | Model: astrocytic and endothelial GLUT1 form a "two-cell gateway" contributing to glucose homeostasis in the brain parenchyma and cerebrospinal fluid (CSF).

Endothelial GLUT1 mediates glucose transport across the blood–brain barrier (BBB). Astrocytic GLUT1, distributed from perivascular endfeet to distal processes, may contribute to maintaining glucose availability within the parenchyma and CSF. Haploinsufficiency of GLUT1 in either compartment is associated with reduced CSF and interstitial fluid (ISF) glucose levels and with cognitive and motor impairments, whereas phenotypic rescue in our experiments required restoration of GLUT1 in both endothelial and astrocytic compartments, consistent with this model. Astrocytes can further metabolize glucose into lactate and supply it to neurons via the astrocyte–neuron lactate shuttle[2,25,26]. Thus, astrocytes may act as central metabolic regulators that shape intracerebral concentration gradients of two major energy substrates—glucose and lactate.

Reference

1. Magistretti, P.J. & Allaman, I. A cellular perspective on brain energy metabolism and functional imaging. *Neuron* **86**, 883–901 (2015).
2. Bonvento, G. & Bolaños, J.P. Astrocyte-neuron metabolic cooperation shapes brain activity. *Cell Metab* **33**, 1546–1564 (2021).
3. Thorens, B. & Mueckler, M. Glucose transporters in the 21st Century. *Am J Physiol Endocrinol Metab* **298**, E141–145 (2010).
4. Veys, K.*, et al.* Role of the GLUT1 Glucose Transporter in Postnatal CNS Angiogenesis and Blood-Brain Barrier Integrity. *Circ Res* **127**, 466–482 (2020).
5. Maher, F., Vannucci, S.J. & Simpson, I.A. Glucose transporter proteins in brain. *Faseb j* **8**, 1003–1011 (1994).
6. De Vivo, D.C.*, et al.* Defective glucose transport across the blood-brain barrier as a cause of persistent hypoglycorrhachia, seizures, and developmental delay. *N Engl J Med* **325**, 703–709 (1991).
7. Leen, W.G.*, et al.* Glucose transporter-1 deficiency syndrome: the expanding clinical and genetic spectrum of a treatable disorder. *Brain* **133**, 655–670 (2010).
8. López-Rivera, J.A.*, et al.* A catalogue of new incidence estimates of monogenic neurodevelopmental disorders caused by de novo variants. *Brain* **143**, 1099–1105 (2020).
9. Symonds, J.D.*, et al.* Incidence and phenotypes of childhood-onset genetic epilepsies: a prospective population-based national cohort. *Brain* **142**, 2303–2318 (2019).
10. Klepper, J.*, et al.* Glut1 Deficiency Syndrome (Glut1DS): State of the art in 2020 and recommendations of the international Glut1DS study group. *Epilepsia Open* **5**, 354–365 (2020).
11. Takahashi, S.*, et al.* The role of molecular analysis of SLC2A1 in the diagnostic workup of glucose transporter 1 deficiency syndrome. *J Neurol Sci* **416**, 117041 (2020).
12. Leen, W.G.*, et al.* Cerebrospinal fluid analysis in the workup of GLUT1 deficiency syndrome: a systematic review. *JAMA Neurol* **70**, 1440–1444 (2013).
13. Ruiz Herrero, J.*, et al.* Classic Ketogenic Diet and Modified Atkins Diet in SLC2A1 Positive and Negative Patients with Suspected GLUT1 Deficiency Syndrome: A Single Center Analysis of 18 Cases. *Nutrients* **13**(2021).
14. Bekker, Y.A.C.*, et al.* Failure of ketogenic diet therapy in GLUT1 deficiency syndrome. *Eur J Paediatr Neurol* **23**, 404–409 (2019).
15. Kramer, J. & Smith, L. Ketogenic Diet in Glut 1 Deficiency Through the Life Cycle: Pregnancy to Neonate to Preschooler. *Child Neurol Open* **8**, 2329048x211034655 (2021).
16. Nakamura, S.*, et al.* Intra-cisterna magna delivery of an AAV vector with the GLUT1 promoter in a pig recapitulates the physiological expression of SLC2A1. *Gene Ther* **28**, 329–338 (2021).
17. Tang, M.*, et al.* An early endothelial cell-specific requirement for Glut1 is revealed in Glut1 deficiency syndrome model mice. *JCI Insight* **6**(2021).
18. Nakamura, S.*, et al.* Gene therapy for a mouse model of glucose transporter-1 deficiency syndrome. *Mol Genet Metab Rep* **10**, 67–74 (2017).
19. Tang, M.*, et al.* Brain microvasculature defects and Glut1 deficiency syndrome averted by early repletion of the glucose transporter-1 protein. *Nat Commun* **8**, 14152 (2017).

20. Pardridge, W.M., Boado, R.J. & Farrell, C.R. Brain-type glucose transporter (GLUT-1) is selectively localized to the blood-brain barrier. Studies with quantitative western blotting and in situ hybridization. *J Biol Chem* **265**, 18035–18040 (1990).
21. Winkler, E.A.*, et al.* GLUT1 reductions exacerbate Alzheimer's disease vasculo-neuronal dysfunction and degeneration. *Nat Neurosci* **18**, 521–530 (2015).
22. Yu, S. & Ding, W.G. The 45 kDa form of glucose transporter 1 (GLUT1) is localized in oligodendrocyte and astrocyte but not in microglia in the rat brain. *Brain Res* **797**, 65–72 (1998).
23. Leino, R.L., Gerhart, D.Z., van Bueren, A.M., McCall, A.L. & Drewes, L.R. Ultrastructural localization of GLUT 1 and GLUT 3 glucose transporters in rat brain. *J Neurosci Res* **49**, 617–626 (1997).
24. Morgello, S., Uson, R.R., Schwartz, E.J. & Haber, R.S. The human blood-brain barrier glucose transporter (GLUT1) is a glucose transporter of gray matter astrocytes. *Glia* **14**, 43–54 (1995).
25. Magistretti, P.J. & Allaman, I. Lactate in the brain: from metabolic end-product to signalling molecule. *Nat Rev Neurosci* **19**, 235–249 (2018).
26. Suzuki, A.*, et al.* Astrocyte-neuron lactate transport is required for long-term memory formation. *Cell* **144**, 810–823 (2011).
27. Challis, R.C.*, et al.* Systemic AAV vectors for widespread and targeted gene delivery in rodents. *Nat Protoc* **14**, 379–414 (2019).
28. Aschauer, D.F., Kreuz, S. & Rumpel, S. Analysis of transduction efficiency, tropism and axonal transport of AAV serotypes 1, 2, 5, 6, 8 and 9 in the mouse brain. *PLoS One* **8**, e76310 (2013).
29. Akman, C.I.*, et al.* Topography of brain glucose hypometabolism and epileptic network in glucose transporter 1 deficiency. *Epilepsy Res* **110**, 206–215 (2015).
30. Nonnenmacher, M.*, et al.* Rapid evolution of blood-brain-barrier-penetrating AAV capsids by RNA-driven biopanning. *Mol Ther Methods Clin Dev* **20**, 366–378 (2021).
31. Ravindra Kumar, S.*, et al.* Multiplexed Cre-dependent selection yields systemic AAVs for targeting distinct brain cell types. *Nat Methods* **17**, 541–550 (2020).
32. Hanlon, K.S.*, et al.* Selection of an Efficient AAV Vector for Robust CNS Transgene Expression. *Mol Ther Methods Clin Dev* **15**, 320–332 (2019).
33. Kunze, C.*, et al.* Synthetic AAV/CRISPR vectors for blocking HIV-1 expression in persistently infected astrocytes. *Glia* **66**, 413–427 (2018).
34. Dewa, K.I.*, et al.* The astrocytic ensemble acts as a multiday trace to stabilize memory. *Nature* **648**, 146–156 (2025).
35. Mendell, J.R.*, et al.* Single-Dose Gene-Replacement Therapy for Spinal Muscular Atrophy. *N Engl J Med* **377**, 1713–1722 (2017).
36. Kawabata, H., Konno, A., Matsuzaki, Y. & Hirai, H. A blood-brain barrier-penetrating AAV2 mutant created by a brain microvasculature endothelial cell-targeted AAV2 variant. *Mol Ther Methods Clin Dev* **29**, 81–92 (2023).
37. Chen, X.*, et al.* Functional gene delivery to and across brain vasculature of systemic AAVs with endothelial-specific tropism in rodents and broad tropism in primates. *Nat Commun* **14**, 3345 (2023).
38. Graßhoff, H.*, et al.* Short regulatory DNA sequences to target brain endothelial cells for gene therapy. *J Cereb Blood Flow Metab* **42**, 104–120 (2022).
39. Vasile, F., Dossi, E. & Rouach, N. Human astrocytes: structure and functions in the healthy brain. *Brain Struct Funct* **222**, 2017–2029 (2017).
40. Matyash, V. & Kettenmann, H. Heterogeneity in astrocyte morphology and physiology. *Brain Res Rev* **63**, 2–10 (2010).

41. Wang, D., *et al.* A mouse model for Glut-1 haploinsufficiency. *Hum Mol Genet* **15**, 1169–1179 (2006).
42. Oddo, M., *et al.* Impact of tight glycemic control on cerebral glucose metabolism after severe brain injury: a microdialysis study. *Crit Care Med* **36**, 3233–3238 (2008).
43. Fray, A.E., Forsyth, R.J., Boutelle, M.G. & Fillenz, M. The mechanisms controlling physiologically stimulated changes in rat brain glucose and lactate: a microdialysis study. *J Physiol* **496**, 49–57 (1996).
44. Dembitskaya, Y., *et al.* Lactate supply overtakes glucose when neural computational and cognitive loads scale up. *Proc Natl Acad Sci U S A* **119**, e2212004119 (2022).
45. Ashrafi, G., Wu, Z., Farrell, R.J. & Ryan, T.A. GLUT4 Mobilization Supports Energetic Demands of Active Synapses. *Neuron* **93**, 606–615.e603 (2017).
46. Carruthers, A. Facilitated diffusion of glucose. *Physiol Rev* **70**, 1135–1176 (1990).
47. Wichmann, T.O., Damkier, H.H. & Pedersen, M. A Brief Overview of the Cerebrospinal Fluid System and Its Implications for Brain and Spinal Cord Diseases. *Front Hum Neurosci* **15**, 737217 (2021).
48. De Giorgis, V., *et al.* Overall cognitive profiles in patients with GLUT1 Deficiency Syndrome. *Brain Behav* **9**, e01224 (2019).
49. Nakamura, S., *et al.* Gene therapy for Glut1-deficient mouse using an adeno-associated virus vector with the human intrinsic GLUT1 promoter. *J Gene Med* **20**, e3013 (2018).
50. Hao, J., Kelly, D.I., Su, J. & Pascual, J.M. Clinical Aspects of Glucose Transporter Type 1 Deficiency: Information From a Global Registry. *JAMA Neurol* **74**, 727–732 (2017).
51. Goyal, M.S. & Raichle, M.E. Glucose Requirements of the Developing Human Brain. *J Pediatr Gastroenterol Nutr* **66 Suppl 3**, S46–s49 (2018).
52. Sakai, K. & Miyazaki, J. A transgenic mouse line that retains Cre recombinase activity in mature oocytes irrespective of the cre transgene transmission. *Biochem Biophys Res Commun* **237**, 318–324 (1997).
53. Pegg, C.C., He, C., Stroink, A.R., Kattner, K.A. & Wang, C.X. Technique for collection of cerebrospinal fluid from the cisterna magna in rat. *J Neurosci Methods* **187**, 8–12 (2010).
54. Ennaceur, A. & Delacour, J. A new one-trial test for neurobiological studies of memory in rats. 1: Behavioral data. *Behav Brain Res* **31**, 47–59 (1988).
55. Georgiou, E., *et al.* Gene therapy targeting oligodendrocytes provides therapeutic benefit in a leukodystrophy model. *Brain* **140**, 599–616 (2017).
56. Carroll, L., Uehara, H., Zhang, X. & Ambati, B. Tropism of the Novel AAVBR1 Capsid Following Subretinal Delivery. *Int J Mol Sci* **23**(2022).
57. Grieger, J.C., Choi, V.W. & Samulski, R.J. Production and characterization of adeno-associated viral vectors. *Nat Protoc* **1**, 1412–1428 (2006).
58. Guo, P., *et al.* Rapid and simplified purification of recombinant adeno-associated virus. *J Virol Methods* **183**, 139–146 (2012).
59. Zolotukhin, S., *et al.* Recombinant adeno-associated virus purification using novel methods improves infectious titer and yield. *Gene Ther* **6**, 973–985 (1999).
60. Yardeni, T., Eckhaus, M., Morris, H.D., Huizing, M. & Hoogstraten-Miller, S. Retro-orbital injections in mice. *Lab Anim (NY)* **40**, 155–160 (2011).